

Making sense of nanocrystal lattice fringes

P. Fraundorf

*Dept. of Physics & Astronomy and Center for Molecular Electronics, U. Missouri-StL, St. Louis MO 63121 USA**

Wentao Qin

Technology Solutions, Freescale Semiconductor, Inc., MD CH305, Chandler AZ 85284 USA

Peter Moeck

Dept. of Physics, Portland State University, P. O. Box 751, Portland OR 97207-0751 USA

Eric Mandell

Dept. of Physics and Astronomy and Center for Molecular Electronics, U. Missouri-StL, St. Louis MO 63121 USA

(Dated: February 1, 2008)

The orientation-dependence of thin-crystal lattice fringes can be gracefully quantified using fringe-visibility maps, a direct-space analog of Kikuchi maps. As in navigation of reciprocal space with the aid of Kikuchi lines, fringe-visibility maps facilitate acquisition of 3D crystallographic information in lattice images. In particular, these maps can help researchers to determine the 3D lattice parameters of individual nano-crystals, to “fringe fingerprint” collections of randomly-oriented particles, and to measure local specimen-thickness with only modest tilt. Since the number of fringes in an image increases with maximum spatial-frequency squared, these strategies (with help from more precise goniometers) will be more useful as aberration-correction moves resolutions into the subangstrom range.

PACS numbers: 87.64.Bx, 87.64.Ee, 81.07.-b

Contents

I. INTRODUCTION

I. Introduction	1
II. Methods	2
III. Observations	2
A. Fringe-visibility bands	2
B. Fringe-visibility maps	3
C. Applications	3
1. Single-particle lattice parameters	3
2. Random particle fringe-fingerprints	5
3. Small-tilt thickness estimates	6
IV. Conclusions	8
Acknowledgments	8
References	9
A. The visibility band outer half-angle	9
B. The inner half-angle critical thickness	10
C. Estimating band intersection areas	11
D. The tilt-range for fringe visibility	11
E. Fringe-visibility rocking curves	12

Nanocrystalline materials have attracted enormous interest due to physical and chemical properties that differ from those of the bulk forms thanks to proper engineering at the atomic level^{1,2}. Phase diagrams and crystal morphologies are frequently dependent on the size of the crystals in the one to ten nanometer size range^{3,4,5}. In addition to this size-dependence for the lowest energy state of a structure, there is a strong tendency in the nanoparticle regime to metastability⁶ and non-stoichiometry. Thus needs for characterization of individual nanocrystals will grow.

A simple approach to determining the lattice (not atomic) structure of nanocrystals, as though they are hand specimens with visible atom columns, was proposed in the late 1980's⁷. It relies on the 3D reconstruction of lattice periodicities from images taken at different tilts. As in diffraction-based techniques^{8,9,10,11,12,13,14} for obtaining 3D crystallographic information, and image-based techniques in stereomicroscopy^{15,16,17,18,19,20,21,22} and electron tomography^{23,24,25,26,27,28,29,30,31}, 3D information is being inferred from slices of 2D projections. As followup, a recent direct determination of lattice parameters in three dimensions from images of a nanocrystal at two tilts³² suggested that such lattice-only analysis strategies could be elegantly visualized using fringe-visibility maps that were quite sensitive to the effects of crystal thickness.

In this paper we investigate visibility, versus orientation, of lattice planes which show up as fringes due to scattering contrast effects when viewed nearly edge-on.

Such fringe contrast occurs for example in electron microscopes under both coherent (phase-contrast) and incoherent (z-contrast) imaging conditions. In this analysis, we concentrate specifically on phase-contrast mechanisms.

Concepts of visibility band, and band maps, are first introduced. Bandwidths are proportional to d-spacing over thickness, rather than to wavelength over d-spacing as in the case of Kikuchi³³, bend-contour^{34,35}, electron-channeling pattern³⁶, and backscatter-electron diffraction³⁷ bands in thicker specimens. Application examples include: 1) image-based protocols for acquisition of 3 linearly-independent lattice plane normals from a single randomly-oriented nanoparticle, each parallel to an operating reflection g-vector, 2) predicting fringe and cross-fringe abundances in a collection of randomly-oriented particles for comparison to experimental data, and 3) measuring local specimen thickness by observing variations in fringe visibility during tilt.

II. METHODS

The transmission electron microscope (TEM) used is a Philips EM430ST with a point resolution just under 0.2 nm. Although lattice-fringe information is often available in electron phase-contrast images out to the “damping limit”, for simplicity we only consider fringes out to the continuous-transfer or “spherical aberration” limit *for a given image* since the absence of smaller fringes may be due to zeros in contrast-transfer. Hence talk here of “point-resolution” limits is shorthand for saying that deductions here consider only fringes whose presence in the sub-specimen electron-wavefield is reliably transferred to the recorded image. Data from two samples were used for experimental measurements of the probability of visualizing {001} zone fringes. The first contained Au/Pd nanocrystals, which were sputtered onto a thin carbon film with a Hummer IV Sputter Coater. The second sample was a nanocrystalline tungsten carbide thin film, deposited by plasma-enhanced chemical vapor deposition (PECVD).

III. OBSERVATIONS

A. Fringe-visibility bands

On tilting away from the edge-on view of a lattice-plane, one encounters a range of incident electron angles (e.g. relative to lattice-plane parallel) within which the lattice plane’s reciprocal lattice spots continue to intersect the Ewald sphere³⁸. Hence lattice fringes associated with those planes remain visible. As shown in Appendix A, the upper bound of this range (with the largest term first in our “thin specimen” limit) is

$$\alpha_{max} = \sin^{-1} \left[\frac{df}{t} + \frac{\lambda}{2d} \left(1 - \left(\frac{df}{t} \right)^2 \right) \right]. \quad (1)$$

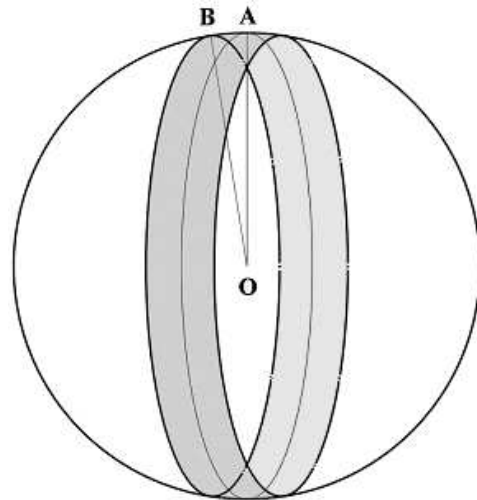


FIG. 1: The visibility band (shaded) of a set of lattice planes of a spherical crystal. Such a band is so defined on a sphere that when the electron beam direction lies in it, the lattice fringes are visible. The great circle running through A is the trace of the lattice plane set. The trace runs through the middle of a visibility band, i.e. the visibility band is symmetric about the trace. The lattice fringes disappear as the electron beam is tilted from any point along the trace in a direction perpendicular to the trace circle by an angle greater than angle $AOB = \alpha_{max}$, the visibility band halfwidth.

Here d is the spacing of lattice planes, t is the crystal thickness, λ is the wavelength of the electrons, and f is a “visibility factor” on the order of 1 that empirically accounts for the signal-to-noise in the method used to detect fringes. The effective radius of the reciprocal lattice spot in this model is f/t . For example, when $f = 1$ this is the first zero in $\sin[\pi gt]/(\pi gt)$: the signal-processing Fourier-transform of a unit-area boxcar function that, convolved with the transform of an infinite lattice, yields the transform of a finite lattice of thickness t . The calculation of α_{max} is based on kinematic conditions. This is also reasonable, since conditions become kinematic when the diffracted beam is about to extinguish.

For much of this paper, we assume that lattice fringes are visible when the electron beam lies parallel to a set of lattice planes. As shown in Appendix B, for thick crystals under parallel illumination this may not be the case for α less than some α_{min} . Our assumption that $\alpha_{min} = 0$ is typically valid for crystals in the 10[nm] and smaller size range.

Two symmetries shall be taken into account when considering lattice fringe visibility versus the incidence direction. The symmetries are: an azimuthal symmetry of the electron beam about the normal of the lattice planes, and a mirror symmetry of the electron beam about the lattice planes. This consideration leads to the concept of fringe visibility band.

Such a visibility band is a schematic representation of an ensemble of electron beam incident directions. These directions are so defined that when the electron beam is

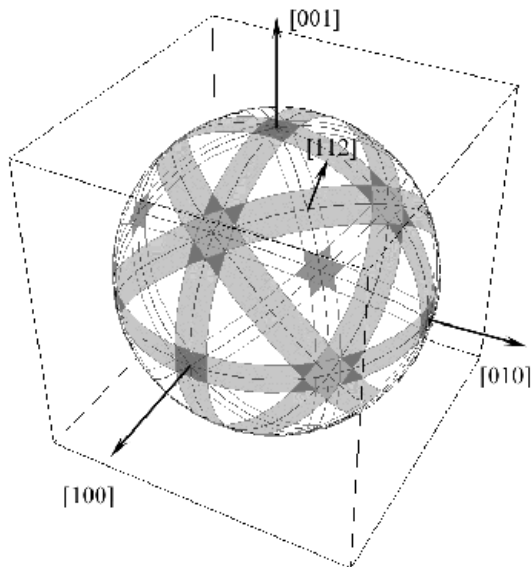


FIG. 2: A fringe-visibility map for a spherical fcc crystal. Each band width is approximately proportional to the corresponding lattice spacing and to the reciprocal lattice spot size. Like Kikuchi maps, fringe-visibility maps reflect crystal symmetry. The latter are of special interest here as a “roadmaps” to guide crystallographic analyses in direct space. For a randomly oriented crystal, the solid-angle subtended by each band is proportional to the probability for the corresponding lattice fringes to be visible, and the solid angle subtended by the cross-section of any two bands is proportional to the probability to get a corresponding zone-axis image.

along any of them, the lattice fringes are visible. As shown in Figure 1, every point on the surface of the sphere simply and elegantly represents a radially inward direction. The ensemble of orientations from which a set of lattice planes is visible form a visibility band on the surface of the sphere. The projection of a lattice plane itself is a great circle, about which the visibility band is symmetric.

For thin specimens and the small λ/d of typical electron microscopes, equation 1 simplifies to $\alpha_{max} \cong \sin^{-1}(df/t) \cong df/t \propto d$. Therefore visibility bands are different from Kikuchi bands in that the band-width is proportional (rather than inversely-proportional) to lattice spacing. Thus we think of visibility bands as tools of “direct space crystallography”.

B. Fringe-visibility maps

The ensemble of all the visibility bands of a spherical crystal forms a fringe-visibility map. The band map not only reveals the crystal lattice symmetry and spacing, but also is TEM-specific, i.e. only resolvable lattice plane sets have their bands on the map. Figure 2 shows such a map. Some examples to appreciate the crystallographic information in fringe-visibility maps are given as follows.

In the figure, four crystal directions are marked. For this cubic lattice, the band perpendicular to the crystal direction of [010] is that of the (020) lattice planes, and that perpendicular to [001] is the band of the (002) lattice planes, etc. The map contains bands of {111}, {002} and {220} lattice planes, with those of the first two classes of lattice plane sets drawn as shaded. The absence of other bands in Fig. 2 suggests that the smallest lattice spacing reliably imaged by the TEM in this model is d_{220} .

C. Applications

As shown in Fig. 3, Kikuchi maps depend primarily on electron wavelength while fringe-visibility maps are affected primarily by specimen thickness. Thanks to the reciprocal nature of diffraction, applications of Kikuchi maps to reciprocal-space exploration are well-known. Crystallographic information in direct-space images is increasingly available. Hence uses for fringe-visibility maps are only beginning to emerge. We discuss only a few here, namely determination of lattice parameters, local measurement of specimen thickness, and “fringe” or “cross-fringe” fingerprinting of randomly-oriented particle collections. A collection of web-interactive maps, using the Mathematica-based Live3D applet by Martin Kraus³⁹, is available here⁴⁰.

1. Single-particle lattice parameters

An efficient way to determine lattice parameters is by acquisition of three lattice vectors whose linear combinations span the entire reciprocal lattice¹². Two of the three vectors may be inferred from a single zone-axis image. For example³² an f.c.c. WC_{1-x} ($a = 4.248$) nanocrystal was examined with a Gatan double-tilt holder ($\pm 15^\circ$ around side-entry goniometer tilt axis, and $\pm 10^\circ$ around the second tilt axis). The fringe-visibility map (reliably seen fringes) involved only the shaded {111} and {002} bands in Fig. 2. Lattice parameters were determined directly from (200), (020) and (11 $\bar{1}$) fringes seen down [001] and [112] zone-axis directions.

This acquisition protocol required a total tilt range of 35.3° . The maximum tilt achievable with the double-tilt holder is 35.6° , barely higher than the tilt required. Because of this limitation only particles at one goniometer extreme, with the correct azimuthal orientation, were candidates for the experiment. Specifically, the [001] zone-axis image was identified from a crystal, among thousands, at the holder setting of $(15^\circ, 9.7^\circ)$. This crystal’s [001] zone was azimuthally oriented so that the [112] zone axis was obtained after tilting to $(-15^\circ, -9.7^\circ)$.

Thus only a small subset of particles using one specific protocol were eligible for this measurement. Improvements in microscope resolution and goniometer range are in the works. Recent progress in resolution enhancement

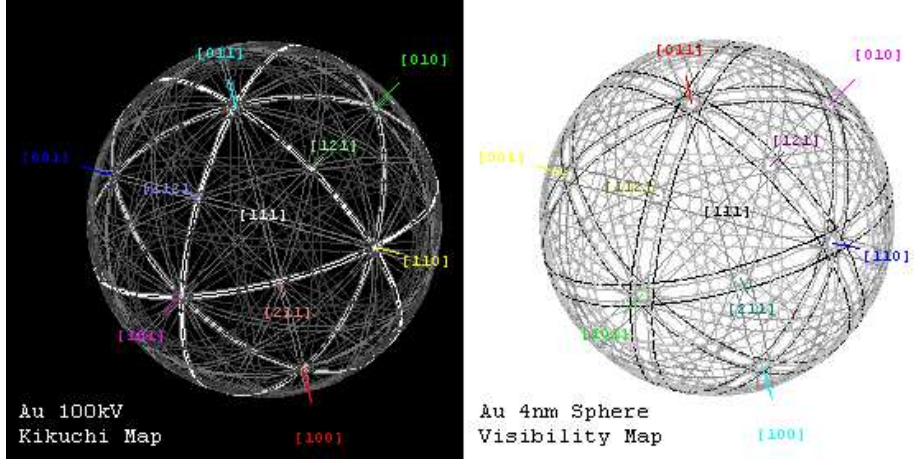


FIG. 3: Comparison of Kikuchi map (left) to a fringe-visibility map (right) for a $t = 4$ [nm] single-crystal gold sphere imaged at 100[kV]. To first order, band-widths in the former (where $t \gg t_{crit}$) are proportional to λ/d , while band-widths in the latter (where $t \ll t_{crit}$) are proportional to d/t . Band boldness and d-spacing are correlated.

by aberration-correction opens up myriad opportunities for image-based nanocrystallography^{41,42,43}. The number of protocols increases at least quadratically with the microscope point-resolution⁴⁴. Accordingly, the fringe-visibility band map will contain more visibility bands and band intersections. Fig. 4 (a) and (b) show fractions of visibility band maps for an 80Å Al-crystal at a point resolution of 1Å, and a 30Å Al-crystal at a point-resolution of 0.6Å, respectively. It is clear that an improvement of continuous contrast transfer results in an increase of the number and width of visibility bands encountered. Thus the choice of protocols to use for lattice parameter determination will multiply, even were the available tilt range to remain fixed. The modified optics of aberration-corrected microscopes will also allow room for a wider range of specimen tilts.

The increase in possible analysis strategies might therefore overwhelm one's hope to “make sense of all those fringes” found on tilting of a randomly-oriented unknown crystal encountered during microscope investigation. As shown in Fig. 4 (c), this is especially problematic if the specimen is very thin. We therefore propose a protocol based on properties of “a fringe-visibility map revealed piecemeal”, as one begins to examine fringes seen in the candidate unknown under initially small exploratory tilts⁴⁵.

The approach is based on one developed for identification of 100[nm] mineral crystallites in an unequilibrated mix by selected area diffraction⁴⁶. It may be broken down into the following steps:

1. Begin with a crystal orientation at which the nanocrystal shows a set of fringes. If no fringes are visible, then the crystal is to be tilted randomly until fringes appear. For example, imagine beginning at the point marked “start” in the fringe visibility band map shown in Figure 5.

2. Tilt the crystal around an axis parallel to the fringes, until the center of the visibility band is located.
3. Tilt the crystal around an axis perpendicular to the fringes, until a cross-fringe intersection (labeled “Zone A” in the map) with another band is encountered.

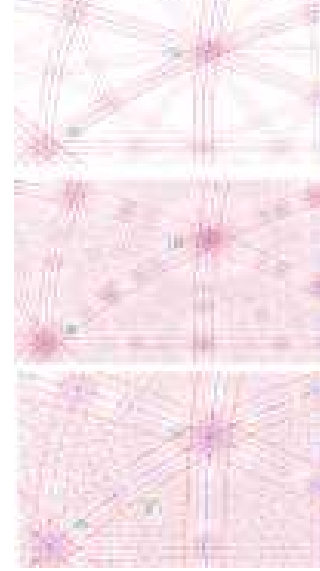


FIG. 4: Visibility band map sections for an 80Å Al-crystal at a point resolution of (a) 1Å, (b) 0.6Å, and (c) 30Å Al-crystal at a point-resolution of 0.6Å. Improvement in point-resolution results in an increase of the number of resolvable lattice planes, and hence that of visibility bands (from a to b). Reduction of crystal size enables visualizing lattice planes over a wider range of angles, so that the width of the bands gets larger (from b to c).

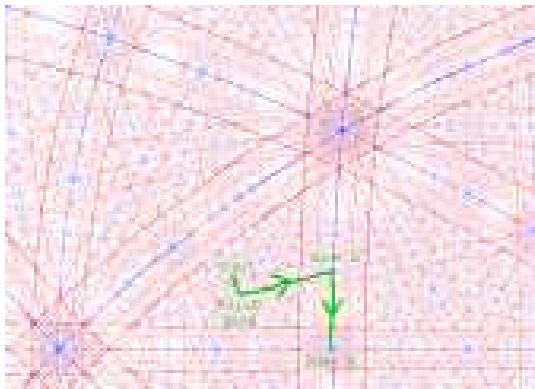


FIG. 5: Visibility band map section at 0.6\AA resolution, showing a trajectory for acquiring three basis fringe (reciprocal lattice) vectors from a randomly oriented unknown. Minimizing beam-direction errors in the measured lattice parameters mandates that as wide a range of tilts as possible be used in the determination.

4. Similarly tilt the crystal around an axis parallel to the second band, until the center of zone A is located. Record lattice spacings and goniometer settings.
5. Tilt the crystal around an axis perpendicular to the second band, until a second cross-fringe intersection (labeled “Zone B” in the map) with the third band is encountered.
6. Repeat the work described in (4) for the third band, to position the beam at the center of that zone and record its positions and lattice spacings as well. Calculate an oriented-basis-triplet i.e. scope coordinates of a randomly-chosen lattice basis¹².
7. Repeat (5)-(6) to include zones at increasingly larger tilt angles as needed to improve accuracy of the oriented-basis-triplet determination.

The basis triplet may at this point be reduced to conventional form, assuming that measurement errors are small enough. The precision of lattice parameter determination can be improved incrementally by measurement of more lattice fringes over a wider range of tilts. Best-fit parameters are easily updated in least-squares fashion as a new set of fringes appear, and each fringe past the first three allows one to estimate the precision in each direction quantitatively. For example, diffraction studies indicate that lattice parameter uncertainties in the beam direction are initially largest, and most dependent on incorporation of spacings observed over a range of tilts¹².

This protocol depends on one’s ability to tilt precisely by small angles in user-chosen directions. Modern double-axis goniometers can do this using computer support, with two caveats: (i) mechanical hysteresis leaves one with a mismatch between goniometer reading and the actual tilt, and (ii) the specimen will move laterally on the nanometer scale. The microscopist can generally

TABLE I: Fringe/Zone probabilities for fcc $a = 4\text{\AA}$; $t = 50\text{\AA}$

	g_{111}	g_{200}	$\frac{p_{uvw}}{\text{zone}}$	# zones
$\langle 110 \rangle$	2	1	.003	6
$\langle 100 \rangle$	0	2	.001	3
$\frac{p_{hkl}}{\text{band}}$.046	.040		
# bands	4	3		

solve the second problem by translating to keep the nanocrystal of interest in the field of view. The problem of tilt hysteresis is more fundamental, and will likely have to be addressed by independent feedback to verify stage orientation at a given instant. Quantitative metrology with scanning probe microscopes requires independent verification of the probe’s lateral position, instead of orientation, but the technologies used there (e.g. optical or capacitive feedback sensing) may be relevant in both cases.

2. Random particle fringe-fingerprints

For a randomly-oriented nanocrystal, the probability that a set of lattice fringes will be visible is simply proportional to the solid angle subtended by the corresponding fringe visibility band. The probability of seeing a pair of cross-fringes is proportional to the solid angle subtended by the corresponding visibility-band intersections. For example, for the randomly oriented spherical f.c.c. nanocrystal whose visibility band map is shown in Figure 2, the probability of seeing (020) lattice planes is equal to the fraction of the 4π solid angle subtended by the (020) visibility band. For cross-fringes along the [001] zone-axis, the probability is equal to the fraction of all solid angles subtended by the cross-section of the two visibility bands centered on the [001] direction.

Thus the probability for seeing a given fringe is simply the whole-band solid angle divided by 4π , or $p_{hkl} = \sin[\alpha_{hkl}]$ where α_{hkl} is α_{max} for $\{hkl\}$ fringes. As shown in Appendix C, the solid angle subtended by a square intersection of bands (from Eqn C3) is approximately $(2\alpha_{max})^2$. Hence the probability of seeing the associated cross-fringe pair is $p_x \cong 2\alpha_{max}^2/\pi$. More generally, for an intersection between a band of halfwidth α_1 and another of halfwidth α_2 at an angle of ϕ , the cross-fringe probability is

$$p_x \cong \frac{2\alpha_1\alpha_2}{\pi \sin[\phi]}. \quad (2)$$

Using a visibility factor of $f = 0.8$ estimated from Au/Pd nanoparticles evaporated on a thin carbon film, p_x for the [100] zone in a WC_{1-x} specimen was predicted to be about $1/700$, consistent with experimental observation⁴⁵. Estimation of such fringe probabilities in turn can be used to quantitatively fingerprint collections of randomly-oriented nanoparticles, according to the fringes and interspot angles in lattice images⁴⁷.

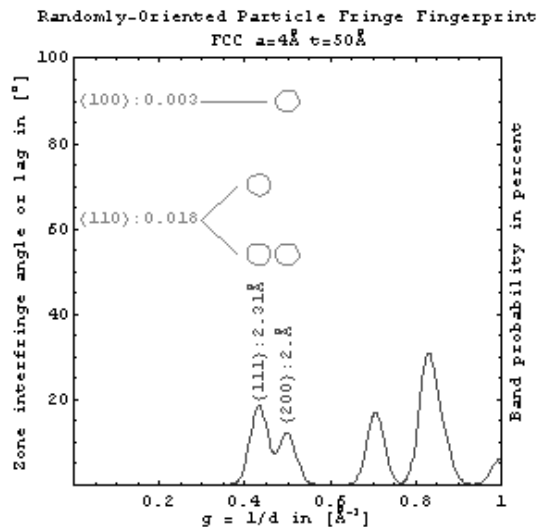


FIG. 6: Template for fringe-visibility fingerprinting of randomly-oriented fcc nano-particle collections. Histogram peak heights equal p_{hkl} , widths equal f/t .

One can begin this process with a probability table for the visible fringes expected from a given type of crystal. For example, Table I lists probabilities expected for the two largest lattice periodicities in a collection of 50Å fcc particles with a lattice parameter or 4Å. Here p_{uvw} is the probability of encountering a fringe-pair for the $[uvw]$ zone. From a table like this, for the system of interest, one can construct a template like that in Fig. 6 for plotting cross-fringe and fringe-histogram⁴⁸ data.

Figure 6 is designed to plot cross-fringe data points (two per spacing pair) and spacing histograms measured manually from multi-particle lattice fringe images. However, it is also patterned after the layout of a fringe angular covariance map⁴⁷. Fluctuation microscopy⁴⁹, used e.g. to characterize medium-range order in paracrystalline specimens⁵⁰, historically has focused on the spacing-only or “powder” component of the pair-pair information available in a combined spatial and angular correlation analysis of image data from complex materials. The layout of Fig. 6, which looks at “patches of correlated periodicity as a function of angular lag” in given size range, also preserves information on the angle between periodicities for such fluctuation analyses. Such plots may therefore prove useful in the automated analysis of HRTEM images as well.

Probability expressions flowing from fringe-visibility maps also allow one to quantify the relative abundance of particles with only one visible fringe, versus those with cross fringes. For example, it nicely explains the fact that 2[nm] particles with cross-fringes are often more abundant than those with single fringes. This is illustrated in Fig. 7, which plots the fraction of particles with $\langle 110 \rangle$ -zone cross-fringes, versus the fraction with only a single $\{111\}$ -fringe showing. Our observations suggest that the size at which this cross-over occurs is quite sensitive to

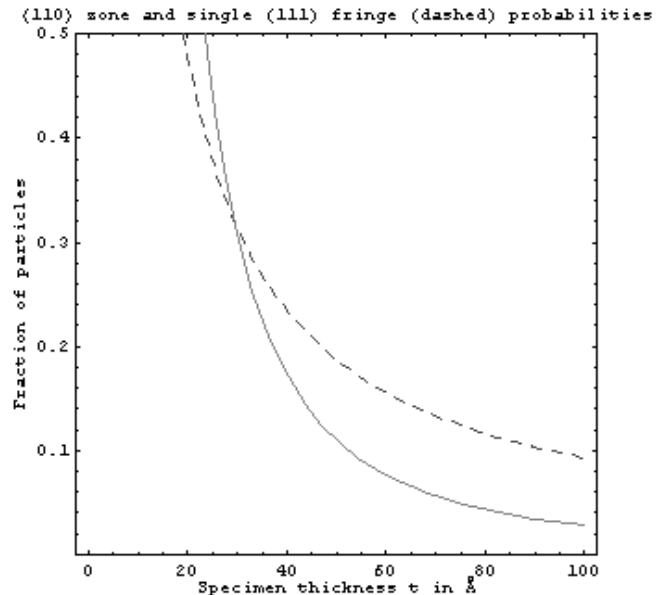


FIG. 7: The cross-over in abundance of cross-fringe versus single-fringe particles, with decreasing size.

viewing conditions, and thus to visibility factor f .

The precision of fringe measurements in such images⁵¹ is limited by shape anisotropy⁵² and other tilt distortions^{53,54,55}. Nonetheless the foregoing analysis works in practice, at least to first order, and provides a framework for more careful study of these deviations as well.

3. Small-tilt thickness estimates

Reduction of crystal size is well-known to result in reciprocal-space broadening of diffraction intensities as seen in X-ray, electron and neutron diffraction. A formula, derived by Paul Scherrer for a thesis on colloids around 1915, correlates such a broadening with the inverse of the mass-weighted average grain size⁵⁶. As shown above, decreasing size causes visibility band broadening as well. Here, we discuss how band broadening can help investigate local specimen thickness.

Given a crystal’s size, lattice, and its orientation with respect to the tilt axis, the tilt-sensitivity of lattice fringe visibility can be predicted. This is done by determining when the reciprocal lattice spot necessarily loses intersection with the Ewald sphere after tilt, given the amount of tilt used and the angle between the fringes and the tilt direction^{57,58}. In order for the reciprocal lattice spot to retain intersection with the Ewald sphere after tilt, the angular deviation of the reciprocal lattice vector from the tilt axis (or equivalently between fringe lines and the tilt direction) must be less than an upper limit ϕ which

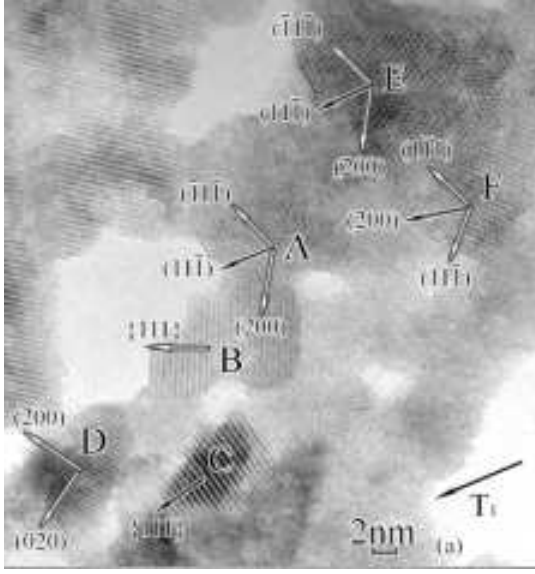


FIG. 8: HRTEM images of six WC_{1-x} nanocrystals showing lattice fringes that become invisible or remain visible after a single tilt of 14.5° around the side-entry goniometer tilt axis. The projection direction of the side-entry goniometer tilt axis T_1 is labeled at the bottom right corner. Each set of parallel lattice-fringes in a nanocrystal has been labeled with both Miller indices and an arrow representing the lattice fringe normal. The length of the arrow is proportional to $1/d$. Here, hollow arrows are used for lattice fringes that are predicted to become necessarily invisible, and solid arrows for those with certain propabilities to do so, in the second specimen orientation shown in Fig 9.

following Appendix D obeys:

$$\sin \left[\frac{\theta_{range}}{2} \right] = \frac{\sin \alpha_{max}}{\sin \phi}. \quad (3)$$

Here α_{max} is given by Eqn 1. If ϕ is the angle between an observed fringe and the tilt direction, then θ_{range} is the tilt-range over which that fringe is visible. Alternatively, if θ_{range} is an experimentally-applied tilt, then fringes whose angle to the tilt direction is more than ϕ will become invisible because their reciprocal lattice spot will necessarily lose intersection with the Ewald sphere after tilt. In this latter application, we will refer to ϕ in equation 3 as ϕ_{max} .

Equations 1 and 3 have been used to predict lattice fringe visibility after tilt for WC_{1-x} nanocrystals as shown in Figure 8. In the figure, each lattice plane set has been labeled with both the Miller indices and an arrow representing the lattice fringe normal. The length of the arrow is proportional to $1/d$. Hollow arrows are used for lattice fringes that are predicted to become necessarily invisible, and solid arrows for those with certain propabilities to do so, after tilt, as shown in the Fig 9. Take those three sets of lattice fringes of crystal A shown in Fig 8, which are those of the WC_{1-x} $(-1,1,-1)$, $(1,1,-1)$ and $(2,0,0)$ lattice planes, as examples. The average

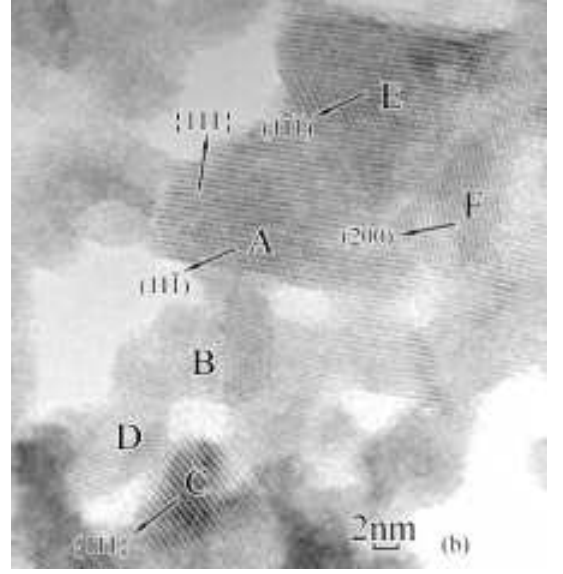


FIG. 9: HRTEM images of the six WC_{1-x} nanocrystals in Fig 8, after a single tilt of 14.5° around the side-entry goniometer tilt axis.

projection size of crystal A is about 48\AA . Equation 3 predicts that for the given amount of tilt

$$\phi(f = 0.79, t = 48\text{\AA}, d_{111} = 2.453\text{\AA}) = 20.6^\circ, \quad (4)$$

and

$$\phi(f = 0.79, t = 48\text{\AA}, d_{002} = 2.124\text{\AA}) = 18.3^\circ, \quad (5)$$

The three lattice fringe normals deviate from the projection of T_1 by 69.1° , 0.3° , 56.6° , respectively. Among them the first and the third are larger than their corresponding limits obtained in equations 4 and 5. Therefore, the $(-1,1,-1)$ and $(2,0,0)$ lattice fringes are predicted to become invisible after tilt. This is shown to be true in Figure 9. This way the invisibility of nine out of thirteen lattice fringe sets are predicted, which is consistent with the HRTEM observation. The results are shown in Table II.

In Figure 8, the nine lattice fringe sets which are predicted to become invisible after tilt are labeled with hollow arrows. Please note that all these lattice fringe sets disappear in Fig 9, which is an indication of the consistency of the model with the HRTEM observations.

Figure 10 shows plots of ϕ_{max} versus thickness with $\theta_{range} = 14.5^\circ$ and $f = 0.79$ for $d_{111} = 2.453\text{\AA}$ and $d_{002} = 2.124\text{\AA}$. Also shown in the figure are the experimental data from Figure 8. Hollow symbols are used to label lattice fringe sets that are observed to become invisible after tilt as shown in Figure 9, and solid symbols for the rest. A consistency between the model and experimental observation is indicated, since all the hollow symbols are above their corresponding curves.

TABLE II: Correlating equation 3 in predicting lattice fringe invisibility after tilt with HRTEM observation as shown in Figures 8 and 9. Quantities in the third and the fifth columns are obtained from Fig 8 before tilt, and column 7 contains a theoretical prediction of invisibility after tilt for comparison to the experimental result from Fig 9 in column 8.

ID	θ°	$t[\text{\AA}]$	(hkl)	ϕ°	ϕ_{max}°	$\frac{\phi}{\phi_{max}} > 1?$	Invisible?
A	14.5	48	(1,1,-1)	0.3	20.6	No	No
			(-1,1,-1)	69.1		Yes	Yes
			(2,0,0)	56.6	18.3	Yes	Yes
B	56	56	(1,1,1)	24.6	17.8	Yes	Yes
C	42	42	(1,1,1)	11.8	23.4	No	No
D	46	46	(2,0,0)	57.5	19.0	Yes	Yes
			(0,2,0)	32.5		Yes	Yes
E	70	70	(1,1,-1)	2.2	14.5	No	No
			(-1,1,-1)	65.0		Yes	Yes
			(2,0,0)	58.2	13.1	Yes	Yes
F	48	48	(1,-1,1)	67.1	20.6	Yes	Yes
			(1,1,-1)	43.9		Yes	Yes
			(2,0,0)	11.8	18.3	No	No

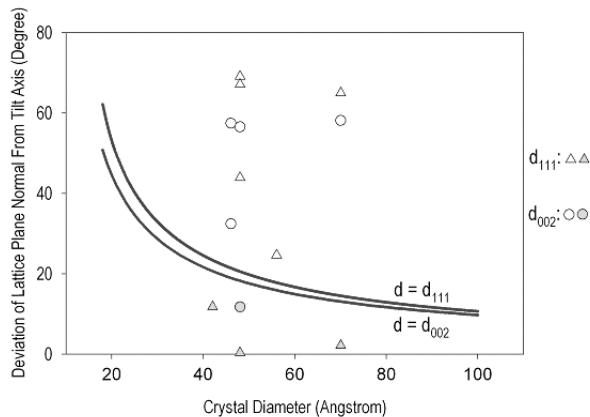


FIG. 10: A plot of the maximum angular deviation of a reciprocal lattice vector from the tilt axis, as given by equation 3, over crystal size. Above such a limit the reciprocal lattice spot necessarily loses intersection with the Ewald sphere after tilting the crystal by 14.5° . Experimental data from Figure 8 and 9 are also shown. The hollow symbols, including both circles and triangles, are used to denote the lattice fringe sets which are observed to become invisible after tilt, and solid symbols for the rest lattice fringe sets. A consistency between the model and the HRTEM observation exists since all the hollow symbols are above their corresponding curves.

Proof of concept in hand, one can easily solve equations 1 and 3 for specimen thickness t . Considering only the dominant term, for example, one gets

$$t \cong df \csc\left[\frac{\theta_{range}}{2}\right] \csc[\phi] \quad (6)$$

where ϕ (as above) is the projected angle between the lattice fringe and the tilt direction. This expression in turn suggests a fractional error in thickness, per unit error in tilt range, of $(1/t)\delta t/\delta\theta \approx t \sin[\phi]/(df)$. For example this predicts a 15 percent error in the thickness, per degree of error in tilt range, for a 50\AA thick foil with a 2\AA fringe twenty degrees from the direction of tilt. This measurement of specimen thickness requires only verification by the microscope operator that tilt range over which the fringe remains visible is about 13 degrees. High precision goniometers, e.g. with verifiable tilt, and a way to profile fringe visibility for small increments in tilt, could thus make it possible to routinely measure nanocrystal thickness at many points in an image with only minor amounts of tilt. With such instrumentation, experimental profiles of fringe intensity as a function of tilt like those modeled in Appendix E could open up a new world of real-time quantitative analysis.

IV. CONCLUSIONS

Fringe-visibility versus orientation for a set of lattice planes, relative to the incident electron beam, in specimens of given thickness is well represented by a “visibility band”. The bands of all lattice planes reliably detected within the point-resolution of a microscope, during a given exposure, make up a fringe-visibility map. Like Kikuchi-maps in reciprocal space, fringe-visibility maps serve as roadmaps for exploring orientation in direct space. We illustrate how they can be useful for determining the 3D lattice parameters of an arbitrary nanocrystal, for fingerprinting fringe and cross-fringe abundances in a collection of randomly-oriented nanocrystals, and for determining the local thickness of crystalline specimens with modest amounts of tilt given a sufficiently precise goniometer. Fringe-visibility maps, and these applications, will be even more useful in aberration-corrected microscopes capable of subangstrom resolution, provided attention is given (during their design) to the precise control *and verification* of specimen orientation.

Acknowledgments

This work has benefited from discussions with L. D. Marks, and indirectly from support by the U.S. Department of Energy and the Missouri Research Board, as well as by Monsanto and MEMC Electronic Materials Companies.

- * pfraundorf@umsl.edu
- ¹ H. Kung and T. Foecke, MRS Bulletin **24**, 14 (1999).
 - ² M. J. Pitkethly, NanoToday pp. 36–42 (2003).
 - ³ W. A. Jesser, G. Shiflet, G. Allen, and J. Crawford, Mat. Res. Innovat. **2**, 211 (1999).
 - ⁴ M. Wautelet, Nanotechnology **3**, 42 (1992).
 - ⁵ M. Wautelet, Nanotechnology **12**, 68 (2001).
 - ⁶ W. M. Tolles, MRS Bulletin **25**, 36 (2000).
 - ⁷ P. Fraundorf, Ultramicroscopy **22**, 225 (1987).
 - ⁸ R. Henderson and P. N. T. Unwin, Nature (2571), 28 (1975).
 - ⁹ R. P. Goehner and P. Rao, Metallography **10**, 415 (1977).
 - ¹⁰ R. Bonnet, J. Microsc. Spectrosc. Electron. **3**, 77 (1978).
 - ¹¹ K.-X. Guo, Acta Phys. Sinica **27**, 160 (1978).
 - ¹² P. Fraundorf, Ultramicroscopy **6**, 227 (1981).
 - ¹³ P. Fraundorf, Ultramicroscopy **7**, 203 (1981).
 - ¹⁴ J. M. Cowley, Journal of Electron Microscopy **45**(1), 3 (1996).
 - ¹⁵ Z. S. Basinski, Proc. 5th International Congress for Electron Microscopy (Academic Press, New York, 1962), vol. 1, p. B13.
 - ¹⁶ Q. Liu, Micron and Microscopia Acta **20**, 261 (1989).
 - ¹⁷ Q. Liu, Q.-C. Meng, and B. Hong, Micron and Microscopia Acta **20**, 255 (1989).
 - ¹⁸ Q. Liu, Micron and Microscopia Acta **21**, 105 (1990).
 - ¹⁹ P. Möck, Cryst. Res. Technol. **26**, 653 (1991).
 - ²⁰ P. Möck, Cryst. Res. Technol. **26**, 797 (1991).
 - ²¹ Q. Liu, X. Huang, and M. Yao, Ultramicroscopy **41**, 317 (1992).
 - ²² P. Moeck and W. Hoppe (Xth European Congress on Electron Microscopy (EUREM 92), 1992), vol. 1, pp. 193–194.
 - ²³ D. J. DeRosier and A. Klug, Nature **217**, 130 (1968).
 - ²⁴ J. M. Cowley, Ultramicroscopy **7**, 19 (1981).
 - ²⁵ L. A. Amos, R. Henderson, and P. N. T. Unwin, Prog. Biophys. Molec. Biol. **39**, 183 (1982).
 - ²⁶ P. Tambuyser, Journal of Materials Science Letters (3), 184 (1984).
 - ²⁷ A. V. Crewe and D. A. Crewe, Ultramicroscopy **16**, 33 (1985).
 - ²⁸ J. Frank and M. Radermacher, in *Advanced techniques in biological electron microscopy*, edited by J. K. Koehler (Springer-Verlag, Berlin, 1986), vol. II, pp. 1–72.
 - ²⁹ H. R. Wenk, K. H. Downing, H. Heisheng, and M. A. O’Keefe, Acta Cryst A **48**, 700 (1992).
 - ³⁰ J. Frank and M. Rademacher, Ultramicroscopy **46**, 241 (1992).
 - ³¹ J. R. Jinschek, H. A. Calderon, K. J. Batenburg, V. Radmilovic, and C. Kisielowski, Mater. Res. Soc. Symp. Proc. **839**, P4.5.1 (2005).
 - ³² W. Qin and P. Fraundorf, Ultramicroscopy **94**(3–4), 245 (2003), cond-mat/0001139.
 - ³³ S. Nishikawa and S. Kikuchi, Nature **121**, 1019 (1928).
 - ³⁴ P. Hirsch, A. Howie, R. B. Nicholson, D. W. Pashley, and M. J. Whelan, *Electron Microscopy of Thin Crystals* (Robert E. Krieger Publishing Company, Huntington, New York, 1977), 2nd ed.
 - ³⁵ L. Reimer, *Transmission electron microscopy: Physics of image formation and microanalysis* (Springer, Berlin, 1997), 4th ed.
 - ³⁶ D. C. Joy, in *Quantitative Scanning Electron Microscopy*, edited by D. B. Holt, M. D. Muir, L. M. Boswarva, and P. R. Grant (Academic Press, New York, 1974).
 - ³⁷ J. A. Venables and C. J. Harland, Phil. Mag. **27**, 1193 (1973).
 - ³⁸ P. P. Ewald, Ann. d. Physik **54**, 519 (1917).
 - ³⁹ M. Kraus, in *the World Wide Web* (<http://www.vis.uni-stuttgart.de/~kraus/LiveGraphics3D/>, 2004).
 - ⁴⁰ P. Fraundorf, in *the World Wide Web* (<http://www.umsl.edu/~fraundorf/nanowrld/live3Dmodels/>, 2004).
 - ⁴¹ M. Haider, S. Uhlermann, E. Schwan, H. Rose, B. Kabius, and K. Urban, Nature **392**, 768 (1998).
 - ⁴² P. Nellist and S. J. Pennycook, Phys. Rev. Lett. **81**(19), 4156 (1998).
 - ⁴³ S. V. Aert, A. J. den Decker, and D. V. Dyck, Micron **35**, 425 (2004).
 - ⁴⁴ P. Moeck, W. Qin, and P. Fraundorf, Mat. Res. Soc. Symp. Proc. **818**, M11.3.1 (2004).
 - ⁴⁵ W. Qin and P. Fraundorf, *On-line determination of nanocrystal lattice parameters* (2003), the 3rd Transmission Electron Aberration-corrected Microscopy Workshop, San Antonio TX.
 - ⁴⁶ P. Fraundorf, Geochim. et Cosmochim. Acta **45**, 915 (1981).
 - ⁴⁷ P. Fraundorf, E. Mandell, W. Qin, and K. Cho, in *Proc. Microscopy and Microanalysis, Savannah GA* (2004), pp. 1262–1263.
 - ⁴⁸ E. Mandell, P. Fraundorf, and M. F. Bertino, in *Proc. Microscopy and Microanalysis, Savannah GA* (2004), pp. 1254–1255.
 - ⁴⁹ P. M. Voyles, J. M. Gibson, and M. M. J. Treacy, Journal of Electron Microscopy **49**, 259 (2000).
 - ⁵⁰ J. M. Gibson and M. M. J. Treacy, Phys. Rev. Lett. **78**, 1074 (1997).
 - ⁵¹ J. Biskupek, U. Kaiser, and A. Chuvilin, Microsc. Microanal. **9** (Suppl. 3), 166 (2003).
 - ⁵² B. E. Warren, Physical Review **59**, 693 (1941).
 - ⁵³ L. D. Marks, Ultramicroscopy **12**, 237 (1983–4).
 - ⁵⁴ J. C. H. Spence, *Experimental High-Resolution Electron Microscopy* (Oxford U. Press, 1988), 2nd ed.
 - ⁵⁵ J.-O. Malm and M. A. O’Keefe, Ultramicroscopy **68**, 13 (1997).
 - ⁵⁶ P. Debye and P. Scherrer, Nachrichten von der Gesellschaft der Wissenschaften zu Göttingen pp. 1–26 (1916).
 - ⁵⁷ W. Qin, Ph.D. thesis, University of Missouri - St. Louis/Rolla (2000).
 - ⁵⁸ W. Qin and P. Fraundorf, in *Proc. 58th Ann. Meeting* (Microscope Society of America, 2000), pp. 1040–1041.
 - ⁵⁹ J. Bailey, *A square’s area after centered plane-projection onto a sphere* (2001), a UM-St. Louis Scanned Tip and Electron Image Lab Project Report.
 - ⁶⁰ H. Hashimoto, A. Howie, and M. J. Whelan, Proc. R. Soc. London Set. A **269**, 80 (1962).

APPENDIX A: THE VISIBILITY BAND OUTER HALF-ANGLE

Figure 11 illustrates the geometry of a simple model for fringe visibility in the center of an equant (e.g. spheri-

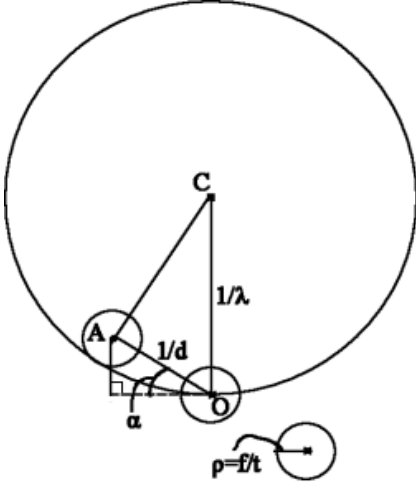


FIG. 11: Ewald sphere geometry for equant-particle fringe visibility. Here **C** is the sphere's center, **O** is the origin of the reciprocal lattice, and **A** is the center of a reciprocal lattice spot.

cal) particle. Visibility requires that the reciprocal lattice “spot” intersect the Ewald sphere. Point **O** is the origin of the reciprocal lattice, and two reciprocal lattice spots are shown a distance $1/d$ away from the center. Since the effective radius of reciprocal lattice spots is affected by many factors, it is written as f/t , where t is the thickness of the crystal and f is a visibility factor. This visibility factor will be a number on the order of 1 that depends on the method of periodicity detection, the range of angles in the illuminating beam, the microscope's response function, and the amount of “fringe obscuring” noise in the field of the image. It may need to be determined experimentally. As a specimen is tilted, the reciprocal lattice spots will come in and out of contact with the Ewald sphere. In Figure 11, the outermost edge of the reciprocal lattice spot is tangent with the Ewald sphere defining a critical angle, α , at which fringes of the corresponding spacing would be viewable in a direct-space image. We derive α as follows.

Since the radius of the Ewald sphere is $1/\lambda$, where λ is the electron wavelength, we can define the length from the center of the Ewald sphere **C** to the center of the reciprocal lattice spot **A** as $1/\lambda - f/t$. The distance from the center of the Ewald sphere to the center of the reciprocal lattice will be $1/\lambda$ and the spacing between the reciprocal lattice spots will be $1/d$. If α is the angle defining the maximum tilt of the reciprocal spot before loss of fringe visibility, then we can use plane trigonometry's Law of Cosines for the complement of angle α in triangle **CAO**, namely

$$\left(\frac{1}{\lambda} - \frac{f}{t}\right)^2 = \frac{1}{d^2} + \frac{1}{\lambda^2} - \frac{2}{d\lambda} \cos\left[\frac{\pi}{2} - \alpha\right], \quad (\text{A1})$$

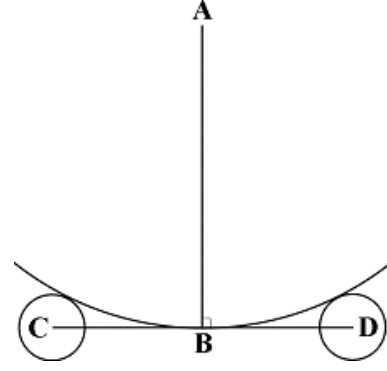


FIG. 12: Schematic configuration with an electron beam traveling down a zone axis, and with reciprocal lattice spots are tangent to the Ewald sphere from the outside. The arc centered at **A** represents part of the Ewald sphere. Segments **BC** and **BD** represent the reciprocal lattice vectors, i.e. $BC = g$ and $BD = -g$. The circles centered at **C** and **D** represent the reciprocal lattice spots. It is obvious **CD** is perpendicular to **AB**.

to obtain

$$\sin[\alpha_{max}] = \frac{df}{t} + \frac{\lambda}{2d} \left(1 - \left(\frac{df}{t}\right)^2\right). \quad (\text{A2})$$

The first term (due to beam-direction broadening of the reciprocal lattice spot) dominates in HRTEM of nanocrystals because d/t is typically greater than λ/d . The equation may also be relevant to electron-channeling, electron-backscatter diffraction, and (with an added factor of 1/2) Kikuchi bands. However, in these cases the λ/d term typically dominates, yielding a $1/d$ rather than d dependence for small-angle band widths.

APPENDIX B: THE INNER HALF-ANGLE CRITICAL THICKNESS

If the specimen is sufficiently thick, or electron wavelengths sufficiently large, images taken with a parallel beam might also show loss of fringe visibility when the specimen is oriented on the zone axis, i.e. between Bragg conditions for diffraction from either side of a set of lattice planes. This condition would introduce an “invisibility stripe” down the center of the visibility band depicted in Fig. 1.

Although the large Bragg angles and thick specimens used for X-ray diffraction make this a common occurrence, it is rare in electron lattice imaging because of the thin nature of the specimens and the small electron wavelength. To confirm this, consider the drawing in Fig. 12. Note that the length of segment **AC** is $1/\lambda + f/t$, the length of segment **BC** is $1/d$, and the length of segment **AB** is $1/\lambda$. Hence from Pythagoras' theorem for right triangle **ABC**, t becomes

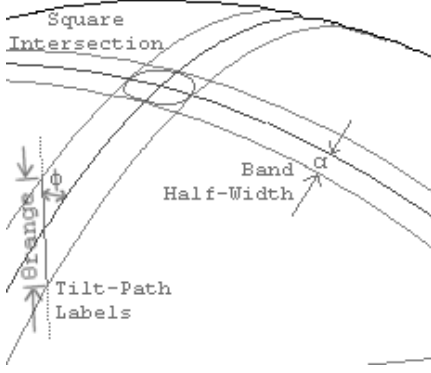


FIG. 13: Visibility bands, a tilt path, and a “cross-fringe” intersection on the surface of a unit sphere.

$$t_{crit} = \frac{fd}{\sqrt{1 + (d/\lambda)^2} - d/\lambda}. \quad (B1)$$

Putting in typical numbers for these quantities shows that this condition is seldom met for specimens thin enough for electron phase contrast imaging, particularly

if effects of beam broadening (i.e. a range of angles in the incident beam) are taken into account. For thicknesses great enough, simply changing the sign of f/t in Eqn. A2 tells us that the half-width α_{min} of the invisibility stripe will obey

$$\sin[\alpha_{min}] = \frac{\lambda}{2d} \left(1 - \left(\frac{df}{t} \right)^2 \right) - \frac{df}{t}, \quad (B2)$$

where the first term is the dominant one.

APPENDIX C: ESTIMATING BAND INTERSECTION AREAS

Consider first the case of equal bands intersecting at right angles, as shown in Fig. 13. We are interested in σ_2 , twice the area σ_1 of one intersection, because great-circle bands intersect twice on opposing sides of the orientation unit sphere. For the inscribed circle shown in the figure, the “double-side solid angle” is $4\pi(1 - \cos \alpha)$. The double-side solid angle of the circumscribed circle is approximately $4\pi(1 - \cos(\sqrt{2}\alpha))$.

For $\alpha < \pi/4$, the *exact* value of the intersection solid angle⁵⁹ is:

$$\sigma_1 = 8 \sum_{n=1}^{\infty} \frac{(-1)^{n+1} \sin[\alpha]^{2n}}{n!} F[n] \prod_{k=1}^n \left(\frac{3}{2} - k \right) = 4\alpha^2 + \frac{2}{9}\alpha^6 + \frac{8}{45}\alpha^8 + \dots, \quad (C1)$$

where hypergeometric function $F[n]$ is

$$F[n] \equiv \sum_{m=0}^{n-1} \frac{(n-1)!}{m!(n-1-m)!} \frac{1}{2m+1}. \quad (C2)$$

For $\alpha > \pi/4$, upper and lower visibility zones connect leaving only four circular “cross-free caps”. Hence σ_1 then becomes $2\pi(2\sin[\alpha] - 1)$.

These observations show that an excellent approximation for small angles is $\sigma_2 \cong 2(2\alpha)^2$, i.e. twice the area one would calculate for a flat square of side 2α . The approximation error is to first order $(4/9)\alpha^6$, and is still below 0.5% when bandwidth 2α is a radian.

More generally, the bandwidth half-angles (e.g. α) follow from the elements described in Appendix A, namely the lattice spacing, specimen thickness, and electron wavelength. When crossing bands have half-angles of α_1 and α_2 , and intersect at an angle of ϕ radians, the flat polygon estimate becomes

$$\sigma_2 \cong \frac{2(2\alpha_1)(2\alpha_2)}{\sin[\phi]}. \quad (C3)$$

Given the value (or an estimate) for visibility-band intersection solid-angles, the probability of seeing cross-fringes in a randomly-oriented particle is then (assuming negligible zone overlap) simply $p_x = n\sigma_2/(4\pi)$, where n is the zone multiplicity e.g. $n=3$ for $\langle 100 \rangle$ zone cross-fringes from a cubic crystal.

APPENDIX D: THE TILT-RANGE FOR FRINGE VISIBILITY

The angular range over which a set of lattice planes remains visible is smallest if the tilt axis is parallel to the planes. Half of this angular range is then given by Eqn. 1. Generally, the tilt axis is not parallel to the lattice planes. To take advantage of band symmetry, we begin with the electron beam initially parallel to the lattice planes as shown in Fig. 14. The tilt range for fringe visibility is then easily quantified.

The figure displays a visibility band segment. A'C' is the trace of the lattice plane. A' is the starting electron beam direction. T is the tilt axis, g is the reciprocal lattice vector. T and g make an angle of ϕ . Since

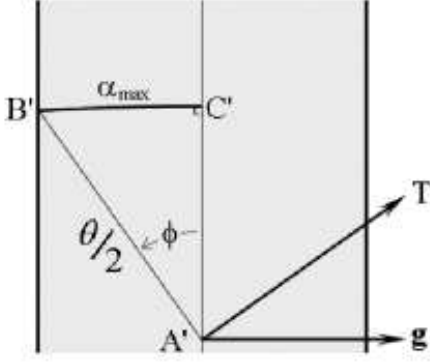


FIG. 14: A segment of a continuous visibility band, with half of the visibility “tilt range” marked by segment A'B'.

$B'C' \perp A'C'$, $B'C' = \alpha_{max}$ is half of the visibility band width. $A'B'$ is the tilt path of the electron beam direction, and is half the total tilt range θ within which the lattice fringes are visible (the other half is symmetric with $A'B'$ about A'). The following relationships are obvious from the figure: $A'B' \perp T$, $\angle B'A'C' = \phi$, and each of $A'B'$, $B'C'$, and $C'A'$ is an arc of a great circle. Spherical trigonometry’s Law of Sines then yields:

$$\sin[\alpha_{max}] = \sin[\phi] \sin[\theta/2]. \quad (D1)$$

APPENDIX E: FRINGE-VISIBILITY ROCKING CURVES

Given the shape of a nanocrystal, the vector separation between a reciprocal lattice point and the Ewald sphere allows one to calculate the Fourier intensity of an individual fringe as a function of orientation. Replacing f/t with g_{sep} in Eqn. 1, and solving, gives for the magnitude of this vector separation

$$g_{sep} = \left| \frac{\sqrt{1 + (\lambda/d)^2 - 2(\lambda/d) \sin[\alpha]} - 1}{\lambda} \right|, \quad (E1)$$

where α is an arbitrary tilt of the beam direction from edge-on.

Because fringe-intensity profiles concern not just the boundaries of fringe visibility, dynamical contrast effects must be taken into account, particularly for crystal thicknesses near to or larger than an extinction distance^{34,35}.

Here, however, we illustrate such profiles or rocking curves for the simplest case, namely a spherical particle of diameter t in the kinematic approximation. For such a particle, the shape transform as a function of spatial frequency g (again using signal-processing conventions) is simply

$$s = \frac{\sin[\pi gt] - \pi gt \cos[\pi gt]}{2\pi^2 g^3}. \quad (E2)$$

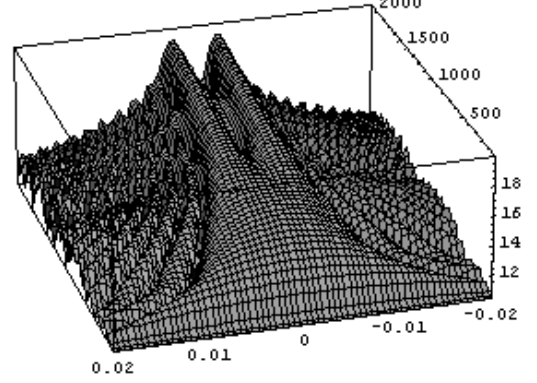


FIG. 15: Logarithmic fringe-intensity profile ($d = 2\text{\AA}$ and $\lambda = 0.01\text{\AA}$) for a spherical particle whose diameter t is given in Angstroms by the top-labeled axis (running front to back), as a function of “tilt from edge-on in radians” on the bottom-labeled axis (running left to right).

Consider a lattice plane canted by α radians from the edge-on position along the electron beam direction. Since all reciprocal lattice spots will be convolved with the shape transform, one can add amplitudes (in the coherent scattering case) from both sides of the lattice plane by adding s -values for g_{sep} evaluated at $\pm\alpha$. Fig. 15 illustrates.

Note that for small thicknesses the fringe intensity profile shows the expected (d/t) -dependence of its angular half-width. For spheres of diameter greater than 650\AA , the rocking curve bifurcates into the fixed (λ/d) -width band cut by the reduced-visibility stripe predicted in Appendix B. This is therefore an alternate view of the transition between thick specimen electron-channeling/Kikuchi map (λ/d) and thin specimen fringe-visibility map (d/t) geometries. Bend-contours of suitably-oriented wedge-shaped crystals thus likely (cf. Fig. 9 Hashimoto et al.⁶⁰) bridge the gap experimentally between both extremes.